Evidence for state dependence of the imaginary part of the empirical optical potential

C. H. Johnson and R. R. Winters*
Oak Ridge National Laboratory, Oak Ridge, Tennessee 37831
(Received 5 October 1987)

From the observed neutron scattering from ^{89}Y and ^{208}Pb at energies from 5 to 10 MeV, there is empirical evidence that the shape of the surface imaginary part of the neutron optical model potential depends upon energy; the radius increases and the diffuseness decreases with decreasing energy. It is shown that the empirical energy dependence for the radius of the surface imaginary potential is approximately the same as that for the positions of the surface nodes for those partial waves which have the same orbital angular momentum l and total neutron angular momentum $j = l \pm \frac{1}{2}$ as for the unoccupied bound single-particle states. The fact that those nodes are clustered near the center of the imaginary potential has the effect of reducing absorption for those partial waves. Therefore, the empirical variation in radius can be reinterpreted by a model for which the radius of the imaginary potential is constant but its strength depends upon the neutron orbital. This dependence can be adequately described by dividing the partial waves into two groups, one with the same quantum numbers l and j as for the bound unfilled orbitals and the other for the unbound states. In the case of n + ^{208}Pb, for an assumed constant imaginary radius, the quality of the optical model descriptions to the data is improved and the dispersion-relation constraint is more nearly satisfied if the partial waves associated with the quasibound single-particle states are also included with those associated with the unoccupied bound single-particle states. However, since the surface nodes for wave functions associated with the quasibound states are not clustered with those associated with the bound states, this optical model potential is not equivalent to the more conventional model which does not have a state dependence but does have an energy-dependent radius for the surface imaginary potential. Furthermore, this model cannot be replaced by one with only a parity dependence in the imaginary potential depth because the parity of the quasibound states is opposite to the parity of the dominant bound states.

I. INTRODUCTION

There have been at least two optical model analyses of neutron scattering data which show an energy dependence in the shape of the surface imaginary component of the neutron optical model potential for energies of a few MeV. Finlay *et al.*[1] and Annand *et al.*[2] found such an energy dependence for scattering from ^{208}Pb, and Lawson *et al.*[3] found it for ^{89}Y. For both cases the radius increases and the diffuseness decreases with decreasing energy.

One influence of the imaginary potential on neutron scattering is described by the transmission factor T_{lj} for neutron orbital angular momentum l and neutron total angular momentum $j = l \pm \frac{1}{2}$. The transmission factor T_{lj} is proportional to an overlap integral[4] of the square of the radial wave function $u_{lj}(r)$ and the imaginary potential, $\mathcal{W}(r;E)$. The empirical imaginary potential is a sum of surface and volume terms. For energies below about 10 MeV the surface term $\mathcal{W}_s(r;E)$ is dominant; therefore, for energies of a few MeV, we have

$$T_{lj}(E) \propto \int \mathcal{W}_s(r;E) \, | \, u_{lj}(r) \, | \, ^2 dr \ . \tag{1.1}$$

Since $\mathcal{W}_s(r;E)$ is peaked near the nuclear surface, the contribution from absorption into the compound nucleus for a given partial wave will be enhanced if $\mathcal{W}_s(r;E)$ is centered near an antinode of the radial wave function; and, in contrast, the contribution will be attenuated if $\mathcal{W}_s(r;E)$ is centered near a node and is narrow relative to the separation of the nodes. The enhancement or attenuation can exhibit a shell effect because the scattering wave functions associated with the orbitals of adjacent major shells are roughly $\pi/2$ out of phase at the nuclear surface.

The importance of the position of $\mathcal{W}_s(r;E)$ relative to the nodes and antinodes was recognized long ago[5] in relation to neutron scattering for low neutron energies, $E < 1$ MeV. In that region the transmission factors can be measured individually for s-wave and p-wave neutrons. The resulting s- and p-wave "size resonances," which appear in plots of strength functions versus A, are interpreted in terms of the overlap integral in Eq. (1.1). Moldauer[6] concluded that, in a mass region where the strength function is near its maximum, the imaginary surface potential is centered near an antinode; whereas, in a mass region where the strength function has it minimum, the imaginary potential is centered near a node. To account for the fact that the minima are quite deep, Moldauer[6] introduced a model with a very narrow surface term in order to adequately attenuate the overlap integral of Eq. (1.1). A recent survey[7] of global models showed that Moldauer's model continues to be better than others for $E < 1$ MeV.

As the neutron energy increases, the positions of the nodes move inward. The relative reduction of absorption

for a given partial wave, either s wave or p wave, persists if the center of $\mathcal{W}_s(r;E)$ tracks inward with the node. Furthermore, other partial waves that are associated with the same major shell will have attenuated effects because the surface radial nodes are clustered in the same radial region for orbitals within a major shell. This phenomenon could also be described by a model in which the radial position of $\mathcal{W}_s(r;E)$ remains fixed while the depth is allowed to be different for partial waves corresponding to different shells. The two depths might be equal at some energy where the surface nodes for one shell are clustered near the peak in $\mathcal{W}_s(r;E)$; if so, the depth for that shell would have to decrease at other energies to compensate for the movement of the clustered nodes away from $\mathcal{W}_s(r;E)$.

Our purpose is threefold. We first show that the empirically derived energy dependences in the radius of the surface imaginary potentials for n + ^{89}Y and for n + ^{208}Pb track the nodes for partial waves which have the same l and j as do the unoccupied bound single-particle states. Secondly, we demonstrate, using n + ^{89}Y as an example, that an equivalent phenomenological description of the data can be achieved using a constant radius for $\mathcal{W}_s(r;E)$ but an lj dependence such that $\mathcal{W}_s(r;E)$ has one depth for partial waves having the same l and j as for the unoccupied bound states and a different depth for the other partial waves. Finally, in the case of n + ^{208}Pb, we refer to a recent study by Johnson, Horen, and Mahaux[8] (henceforth JHM) in which the dispersion-relation constraint[9] (DR) was invoked to develop a mean field for n + ^{208}Pb for a very broad energy region from −20 to 165 MeV. In that study it was found that the description of the scattering data[1,2] for energies of a few MeV can be improved if the depth of $\mathcal{W}_s(r;E)$ is given a modified shell dependence in which the partial waves with lj associated with single-particle states that are quasibound by the centrifugal barrier are grouped along with those associated with the bound single-particle states. This modified state dependence is not equivalent to an energy-dependent radius because the nodes for the partial waves associated with the quasibound states do not cluster with those associated with the bound single-particle states. We review this modified shell dependence and find that it not only gives a good description of the data but also is more nearly consistent with the DR constraint than are various other models.

In Sec. II we define notations to be used throughout the paper. In Sec. III we discuss the case of n + ^{89}Y. In Sec. IV we discuss the empirical energy-dependent geometry for n + ^{208}Pb, and in Sec. V we discuss the empirical state dependence for that nucleus. Section VI is our conclusion.

II. THE NOTATIONS "B" AND "U"

The nuclei ^{89}Y and ^{208}Pb have closed neutron shells and have similar structures for the bound states of the next unoccupied major shell. The nucleus ^{89}Y has 50 neutrons; the even parity states of the next major shell are $3s_{1/2}$, $2d_{3/2}$, $2d_{5/2}$, and $1g_{7/2}$, and the only odd parity state is $1h_{11/2}$. The ^{208}Pb has the next two major shells filled to give 126 neutrons; hence, the structure of the next major unoccupied shell is similar to that for ^{89}Y, except for the increase of one unit in principal quantum number. The even parity states for ^{208}Pb are $4s_{1/2}$, $3d_{3/2}$, $3d_{5/2}$, $2g_{9/2}$, $2g_{7/2}$, and $1i_{11/2}$; the only odd parity state is $1j_{15/2}$.

In Secs. III and IV, we use the notation "B" to designate neutron wave functions which have the same quantum numbers l and j as for bound single-particle states of the next unoccupied major shell. *These are scattering wave functions; in no case do we discuss bound-state wave functions.* In Sec. V we expand the definition of B to include partial waves for which l and j are the same as for single-particle states that are quasibound by the centrifugal barrier. These scattering wave functions are not the wave functions of the quasibound states, except in the special case where the neutron energy coincides with the energy of the quasibound state. In all sections the letter "U" will designate the remaining partial waves, which have lj associated with "unbound" states.

III. MODEL FOR n+^{89}Y

Lawson *et al.*[3] analyzed the experimental scattering distributions for 1.5- to 10-MeV neutrons on ^{89}Y using a conventional optical model consisting of a central real component of Woods-Saxon shape, a spin-orbit term of the Thomas form, and an imaginary component of the Woods-Saxon derivative shape. (We do not discuss their other model, which had a real surface dispersive term.) We are interested particularly in their surface imaginary term, which has the Woods-Saxon derivative shape,

$$\mathcal{W}_s(r;E)=-4a_s(E)W_s(E)d/drf[X_s(E)] , \tag{3.1}$$

where

$$f[X_s(E)]=\{1+\exp[X_s(E)]\}^{-1} , \tag{3.2a}$$

$$X_s(E)=[r-R_s(E)]/a_s(E) , \tag{3.2b}$$

$$R_s(E)=r_s(E)A^{1/3} . \tag{3.2c}$$

The analysis[3] for 5- to 10-MeV neutrons gave the following energy dependences in fermis:

$$r_s(E)=1.5336-0.0255E , \tag{3.3}$$

$$a_s(E)=0.1661+0.0284E , \tag{3.4}$$

where the neutron energy E is in MeV. The volume integral per nucleon was found to be independent of energy;

$$J_{W_s}/A=-66.47\pm1.29 \text{ MeV fm}^3 . \tag{3.5}$$

The curves in Fig. 1 represent radial wave functions, $u_{lj}(r)$, calculated at $E=5$ MeV from the real part of the potential[3] and normalized to unit amplitude at large radii for partial waves $l=0$ to 5. The U and B scattering wave functions are represented in Figs. 1(a) and 1(b), respectively. The dashed curves represent the shape of the surface imaginary potential $\mathcal{W}_s(r;E)$ from (3.1). We see that *nodes* for the B partial waves cluster near R_s, whereas *antinodes* for the other partial waves are near R_s.

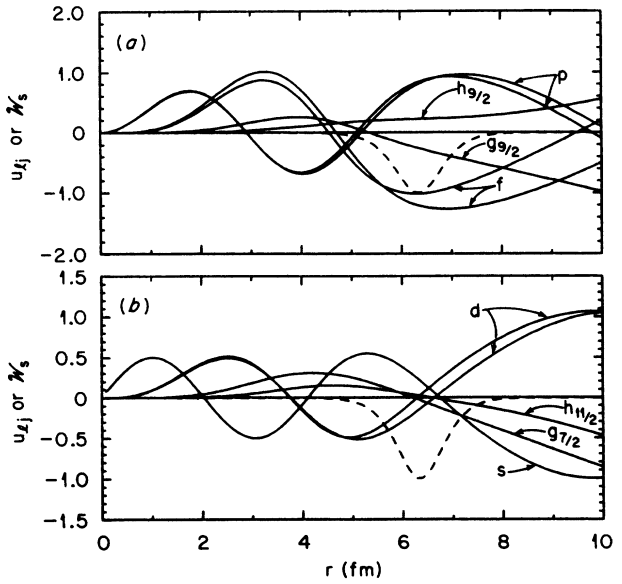

FIG. 1. Radial scattering wave functions $u_{lj}(r)=rR_{lj}(r)$ calculated at 5 MeV for n + ^{89}Y using the real part of the potential from Ref. 3. The curves in (b) represent partial waves having the same quantum numbers l and j as do the bound unoccupied single-particle states in ^{90}Y; the curves in (a) represent the other partial waves. The wave functions are normalized to unit amplitude at large radii. The dashed curves represent the surface imaginary potential, with arbitrary normalization.

It follows from Eq. (1.1) that the absorption effects are attenuated for the B partial waves.

In Fig. 2 the solid curves represent the energy dependences of the radial positions, r_{node}, of the surface nodes. The upper five curves are for the B scattering wave functions. The dashed curve represents the energy dependence of the imaginary radius $R_s(E)$, Eq. (3.3). We see that this empirical radius closely tracks the clustered nodes of the B scattering wave functions. Therefore, the reduction of absorption for partial waves which have the same lj as do the unoccupied bound single particle states persists over an energy region of several MeV.

The empirical energy dependence in the imaginary radius can be replaced by a state dependence in the depth of the imaginary potential. To demonstrate, we assume such a model for n + ^{89}Y and deduce an equivalent potential for 5-MeV neutrons. For the real and spin-orbit potentials we use the same parametrizations as for the original models.[3] For the surface imaginary potential we assume a constant shape by evaluating Eqs. (3.3) and (3.4) for $E=10$ MeV;

$$r_s=1.28 \text{ fm and } a_s=0.45 \text{ fm} . \tag{3.6}$$

However, we allow different energy dependences in the depths for the B and U partial waves;

$$\mathcal{W}_{sB}(r;E)=-4a_s W_{sB}(E)d/drf(X_s) , \tag{3.7}$$

$$\mathcal{W}_{sU}(r;E)=-4a_s W_{sU}(E)d/drf(X_s) . \tag{3.8}$$

We first calculate the shape of elastic scattering distribution predicted at 5 MeV by the published model;[3] the resulting distribution is represented by the solid curve in Fig. 3. Next we treat the cross sections from this distribution as "data" and search by least squares on W_{sB} and W_{sU}. The resulting W_{sB} and W_{sU} are 3.88 and 8.70 MeV, respectively. As expected, the depth W_{sB} has been significantly reduced relative to W_{sU} in order to reduce absorption for B partial waves. The resulting scattering distribution, which is represented by the dashed curve in Fig. 3, agrees well with the solid curve.

At this point we do not suggest that one or the other of these equivalent parametrizations is preferred. In fact, it could be that some other grouping of the partial waves could achieve a better fit than either of these "equivalent" models. That is the subject of Sec. V in regard to n + ^{208}Pb.

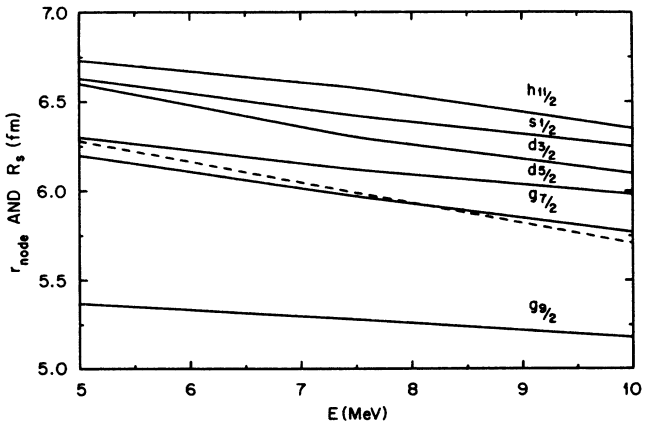

FIG. 2. Energy dependences of the positions of the surface nodes of $u_{lj}(r)$ calculated as in Fig. 1. The solid curves represent the positions of the nodes and the dashed curve represents the energy dependence of the imaginary potential radius $R_s(E)$ from Eqs. (3.2c) and (3.3).

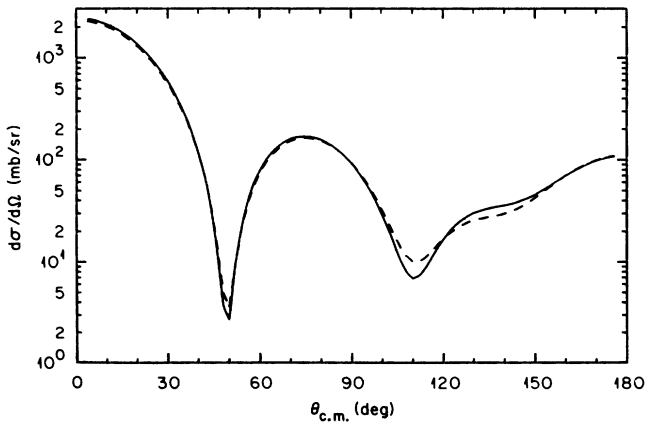

FIG. 3. Shape elastic angular distributions for alternate models for 5-MeV neutron scattering from ^{89}Y. The solid curve is calculated from the conventional optical model of Ref. 3. The dashed curve represents a fit to the solid curve using the state-dependent model discussed in Sec. III.

IV. THE n+^{208}Pb MEAN FIELD

The optical model analyses of Refs. 1 and 2 showed that the shape of the surface imaginary component of a conventional local optical model potential is energy dependent in the case of neutron scattering from ^{208}Pb. More recently those experimental data for ^{208}Pb were incorporated into a broad study by JHM (Ref. 8) which led to a unified description of the neutron-^{208}Pb mean field for energies from -20 to $+165$ MeV. This unified description was achieved by imposing the DR constraint,[9] which connects the real and imaginary parts of the field. The imaginary field is the sum of surface and volume terms, but the volume term is negligible for scattering below 10 MeV, which is the region of particular interest here. The dispersive contribution $\Delta\mathcal{V}_s(r;E)$ to the real potential from the surface term is given by

$$\Delta\mathcal{V}_s(r;E)=\pi^{-1}\int_{-\infty}^{+\infty}dE'\mathcal{W}_s(r;E')/(E'-E)\ . \quad (4.1)$$

where the principal value integral is to be calculated.

A difficulty with the integral in Eq. (4.1) is that it can be evaluated in algebraic form for only a limited set of functional forms for $\mathcal{W}_s(r;E)$. In particular, an energy dependence in the radial shape of $\mathcal{W}_s(r;E)$ would not yield a Woods-Saxon derivative shape for $\Delta\mathcal{V}_s(r;E)$. The study by JHM (Ref. 8) was done primarily with the approximation that all of the potential shapes are independent of energy. With that assumption, the DR involves only the well depths of the potentials. In particular, the surface potentials, $\Delta\mathcal{V}_s(r;E)$ and $\mathcal{W}_s(r;E)$, have the same shape and the DR reduces to an equation for the well depths,

$$\Delta V_s(E)=\pi^{-1}\int_{-\infty}^{+\infty}dE'W_s(E')/(E'-E)\ . \quad (4.2)$$

The surface shape parameters determined by JHM (Ref. 8) are

$$r_s=1.27\ \text{fm} \quad (4.3)$$

and

$$a_s=0.58\ \text{fm}\ . \quad (4.4)$$

With this model[8] a remarkable description of a large body of data was achieved over a broad energy range from -20 to $+165$ MeV. Even so, there remained evidence that the shape of the surface imaginary potential should be allowed to vary with energy for $E<10$ MeV. In fact, in Sec. VI of JHM (Ref. 8) the shape of $\mathcal{W}_s(r;E)$ was allowed to vary, and an energy dependence was found similar to that deduced in the original publications[1,2] of the low energy data. For the experimental region, $4<E<10$ MeV, the dependences were described by JHM (Ref. 8) by the equations

$$r_s(E)=1.46-0.0189E\ \text{fm}\ , \quad (4.5)$$

$$a_s(E)=0.067+0.0513E\ \text{fm}\ , \quad (4.6)$$

where E is in MeV.

This empirical energy dependence in the shape of $\mathcal{W}_s(r;E)$ for n + ^{208}Pb is quite similar to that quoted in Sec. III for n + ^{89}Y. Furthermore, there are striking similarities between the two nuclides in regard to the position of the surface potential relative to the nodes of the radial wave functions. The solid curves in Fig. 4 represent radial wave functions calculated at 10 MeV from the real part of the potential that was developed by JHM (Ref. 8) in connection with Eqs. (4.5) and (4.6). The B and U scattering wave functions are presented in Figs. 4(a) and 4(b), respectively. [The $j_{15/2}$ partial wave is omitted from Fig. 4(a) because the contributions to the scattering are negligible for $l>6$.] The dashed curves represent the shape of $\mathcal{W}_s(r;E)$. Here, as in Fig. 1, the empirical imaginary potential is centered near the surface nodes for the B wave functions. In Fig. 5 the solid curves represent the variations in the positions of these surface nodes for $5<E<10$ MeV. The dashed curve represents the empirical energy dependence for the imaginary radius $R_s(E)$. We see here, as for ^{89}Y in Fig. 2, that $R_s(E)$ tracks the surface B nodes. We expect, therefore, that the empirical energy dependence $R_s(E)$ could be replaced by a shell or state dependence in the depth.

V. STATE DEPENDENCE FOR n+^{208}Pb

In Sec. VII of JHM (Ref. 8) the scattering distributions for n + ^{208}Pb were analyzed once more for $E<10$ MeV using the constant $r_s=1.27$ fm, Eq. (4.3), but allowing the depth of the imaginary potential to depend on the quantum numbers of the partial waves. The partial waves were separated into two groups; however, these were not B and U, as suggested above, but groupings of l values which were chosen to give the best fits to the data.

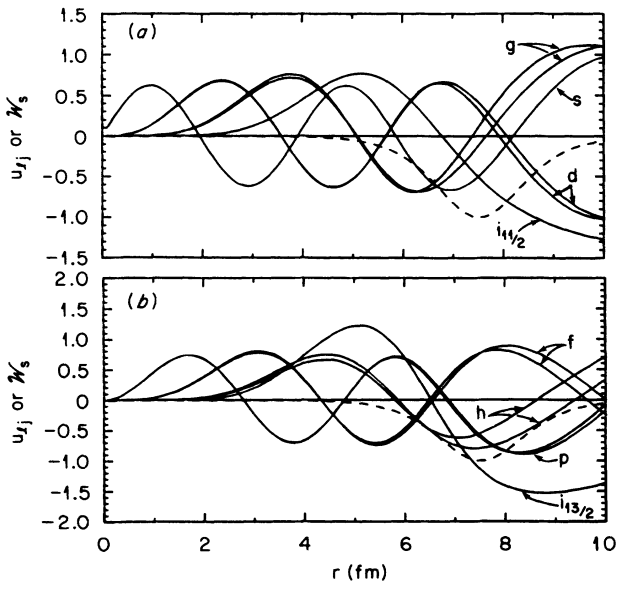

FIG. 4. Neutron scattering radial wave functions u_{lj} calculated for n + ^{208}Pb at 10 MeV using the real part of the optical model potential developed in Sec. VI of Ref. 8. The curves in (a) represent partial waves which have the same lj as do the bound unoccupied single-particle states in ^{209}Pb; the curves in (b) represent the other partial waves. The dashed curves represent the surface imaginary potential, with arbitrary normalization.

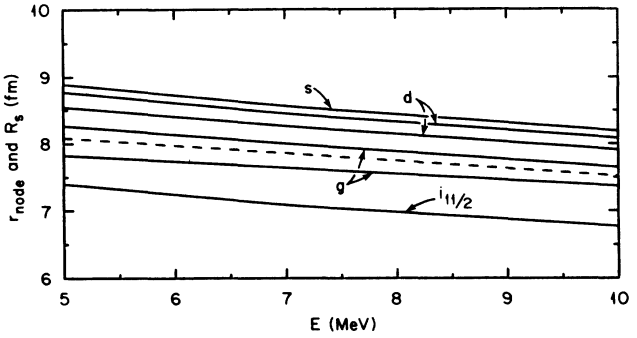

FIG. 5. Energy dependences of the surface nodes of the radial wave functions calculated as in Fig. 4(a). The solid curves represent the positions of the nodes and the dashed curve represents the imaginary potential radius $R_s(E)$, from Eqs. (3.2c) and (4.5).

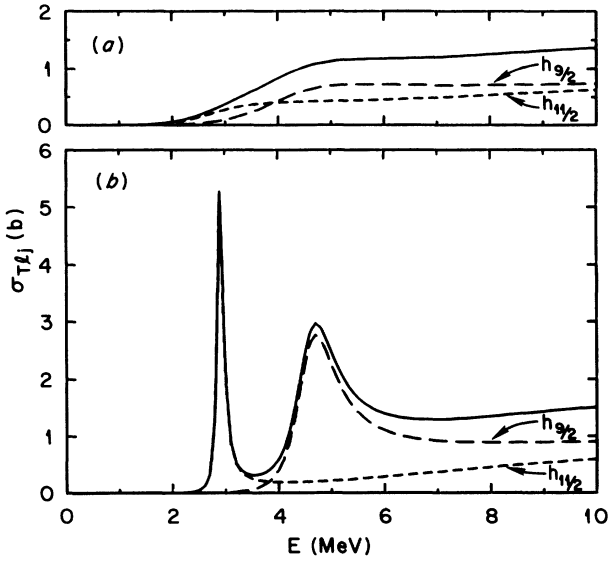

FIG. 6. Angle-integrated cross sections for the n + ^{208}Pb partial waves with $l=5$. The short-dashed and long-dashed curves represent cross sections for $h_{11/2}$ and $h_{9/2}$ partial waves, respectively, and the solid curves represent the total for h waves or $l=5$. The curves in Fig. 6(a) are calculated for the "optimum" model described in Sec. V and the curves in Fig. 6(b) are calculated from the real part of that model.

In fact, the resulting empirical grouping[8] yields better fits than obtained by the model of Sec. IV with its energy-dependent radius. This new model[8] has the partial waves for $l=1$, 3, and 6 in one group, designated "b" by JHM, and all other l values in a second group, designated "c." This c and b grouping would be transformed to the B and U groupings, respectively, if $i_{11/2}$ were moved from b to c and $h_{9/2}$, $h_{11/2}$, $j_{15/2}$, and $l>7$ were all moved from c to b. However, this transformation would cause the quality of fits to deteriorate such that the transformed model would be no better than the one with the energy-dependent radius. The deterioration does not result from moving the $i_{11/2}$, $j_{15/2}$, and $l>7$ partial waves from one group to the other; those transfers have negligible effects on the predicted scattering distributions. It is the transfer of the $l=5$ partial waves which worsens the quality of fits. A primary purpose of the present section is to gain a better understanding of the special role of the partial waves with $l=5$.

For our version of the "optimum" model we transfer only the partial waves which do not disturb the quality of fits. Thus the definition of B is now expanded from that used in Secs. III and IV; it includes not only the $s_{1/2}$, $d_{3/2}$, $d_{5/2}$, $g_{7/2}$, $g_{9/2}$, $i_{11/2}$, and $j_{15/2}$ partial waves, i.e., those with the same lj as for the unoccupied single-particle bound states, but also the odd parity $h_{9/2}$ and $h_{11/2}$ partial waves. From the viewpoint of a strict neutron shell dependence, the $h_{9/2}$ and $h_{11/2}$ partial waves are intruders into the B group. In Fig. 4 the $h_{9/2}$ and $h_{11/2}$ wave functions are included in the lower figure rather than the upper figure; they have antinodes rather than nodes near the nuclear surface. On the other hand, h waves are kindred to the bound particle orbits because the h-wave single-particle states are quasibound, as we now show.

In Fig. 6(a) the solid curves represent the angle-integrated cross section for $l=5$ calculated from the model, and the dashed curves represent the corresponding $h_{9/2}$ and $h_{11/2}$ components. In Fig. 6(b) the curves represent the cross sections predicted from only the real part ($W_s=0$) of the potential. The latter curves show that, in the absence of the spreading due to $\mathcal{W}_s(r;E)$, the $h_{11/2}$ and $h_{9/2}$ cross sections exhibit well defined resonances at energies where the scattering phase shifts pass through $\pi/2$. The peak cross sections are $4\pi g_j/k^2$, where g_j is the statistical factor; the energies of the peaks are 2.9 MeV for $h_{11/2}$ and 4.75 MeV for $h_{9/2}$. These resonances occur because the $2h_{9/2}$ and $2h_{11/2}$ states are quasibound by the centrifugal barrier. In Fig. 7 the curves represent the total real potentials found by sum-

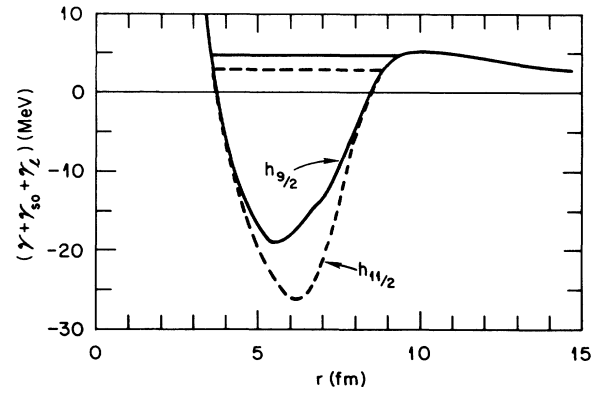

FIG. 7. Total real potentials and quasibound states for h-wave neutrons on ^{208}Pb. The solid and dashed curves represent sums of the dispersive, spin-orbit, centrifugal, and real central components for the "optimum" potential discussed in Sec. V, and the solid and dashed horizontal lines drawn within these potentials represent the energies of the $h_{11/2}$ and $h_{9/2}$ resonances shown in Fig. 6. The potentials are calculated at the neutron energies of the resonances.

ming the centrifugal, spin-orbit, dispersive, and central Woods-Saxon components of the model. The dashed curve is calculated at the $2h_{11/2}$ resonance energy using the spin-orbit potential for $h_{11/2}$, and the solid curve is calculated at the $2h_{9/2}$ resonance energy using the spin-orbit term for $h_{9/2}$. The corresponding solid and dashed horizontal lines represent the energies of the $2h_{9/2}$ and $2h_{11/2}$ resonances. The $2h_{11/2}$ state is relatively tightly bound so that the resonance width in Fig. 6(b) is narrow, whereas the $2h_{9/2}$ state is just below the centrifugal barrier such that its width is large and its position is not so well defined.

We study the roles of the various partial waves by making a series of least-squares searches on the data[1,2,10–12] for $4<E<14$ MeV, using various perturbations of the orbital groupings of our optimum model. Obviously we cannot consider all possible perturbations and so we consider only those for which the B partial waves, as originally defined in Sec. II, are kept together in the same group. The spin-orbit and volume potential parameters are held constant at the values of the "fixed geometry" model described in Secs. II and III of JHM.[8] The spin-orbit parameters are given in Eq. (2.2) of JHM,[8] the shape parameters for the central Woods-Saxon potential are given in Eqs. (3.1) and (3.3) of JHM,[8] and the central depths are represented by the solid curves in Fig. 2 of JHM.[8]

There are now two surface DR equations corresponding to groups B and U:

$$\Delta\mathcal{V}_{sB}(r;E)=\pi^{-1}\int_{-\infty}^{+\infty}dE'\mathcal{W}_{sB}(r;E')/(E'-E)\ , \quad (5.1)$$

$$\Delta\mathcal{V}_{sU}(r;E)=\pi^{-1}\int_{-\infty}^{+\infty}dE'\mathcal{W}_{sU}(r;E')/(E'-E)\ . \quad (5.2)$$

We assume that the two imaginary potentials have the same derivative Woods-Saxon shape:

$$\mathcal{W}_{sB}(r;E)=-4a_s(E)W_{sB}(E)d/drf[X_s(E)]\ , \quad (5.3)$$

$$\mathcal{W}_{sU}(r;E)=-4a_s(E)W_{sU}(E)d/drf[X_s(E)]\ , \quad (5.4)$$

where the radius is constant, $r_s=1.27$ fm.

Since r_s is assumed to be constant, the dispersive terms on the left-hand sides of Eqs. (5.1) and (5.2) remain symmetric about the same radius as for the imaginary potential; however, these terms cannot be represented by derivative Woods-Saxon shapes if the diffuseness $a_s(E)$ is energy dependent. In some cases the deviation from the derivative shape can be significant.[13] We assume, nevertheless, that the effect of the dispersive term can be approximated using a derivative Woods-Saxon shape with the same diffuseness, $a_d(E)$ for both groups;

$$\Delta\mathcal{V}_{sB}(r;E)=-4a_d(E)\Delta V_{sB}(E)d/drf[X_d(E)]\ , \quad (5.5)$$

$$\Delta\mathcal{V}_{sU}(r;E)=-4a_d(E)\Delta V_{sU}(E)d/drf[X_d(E)]\ . \quad (5.6)$$

We believe that this approximation is a good basis for intercomparison of the various perturbations of the model. The diffuseness functions $a_d(E)$ and $a_s(E)$ were deduced[8] by including a_d and a_s as variables in six-parameter searches. The resulting values of a_s are well described by Eq. (4.6). However, the resulting values of a_d show[8] considerable variation; for energies from 4 to 7 MeV the values are about 0.4 fm, but for 9, 10, and 11 MeV they are very large, 3 to 4 fm with large uncertainties. We use the following approximation:[8]

$$a_d(E)=0.34+0.024E \text{ fm} \quad \text{for } 4<E<10 \text{ MeV}\ , \quad (5.7a)$$

$$a_d(E)=a_s(E)=0.58 \text{ fm} \quad \text{for } E>10 \text{ MeV}\ , \quad (5.7b)$$

and later in this section we return to the fact that, for energies near 10 MeV, these equations are inconsistent with the large empirical values which give the minimum χ^2/N.

The DR constraint is not imposed during the searches on the parameters of the imaginary potential because the energy dependences of $\mathcal{W}_{sB}(r;E)$ and $\mathcal{W}_{sU}(r;E)$ are required prior to evaluating the dispersion integrals. The procedure is to adjust the well depths W_{sB}, W_{sU}, ΔV_{sB}, and ΔV_{sU} for both imaginary and dispersive components and, after determining optimum values, to check for consistency with the DR constraints.

Searches are made for the "optimum" model and three perturbations.

M. The "optimum" model for which B includes partial waves associated with the bound orbits and with the quasibound h orbits. All other partial waves are in U.

*P*1. The same as *M* except $h_{9/2}$ is moved from B to U.

*P*2. The same as *M* except that both $h_{11/2}$ and $h_{9/2}$ are moved from B to U.

*P*3. Only the $h_{11/2}$ and $h_{9/2}$ partial waves are in B. All others are in U.

We compare the results of the least-squares searches on the basis of three criteria: (i) the quality of fits as indicated by the least-squares χ^2/N for the scattering distributions[1,2,10–12] from 4 to 14 MeV, (ii) the relative values of the fitted imaginary well depths, and (iii) the consistency of the fitted real surface depths with the DR constraint.

In Fig. 8 the four symbols represent the values of χ^2/N, where N is the number of data points for a scattering distribution at a given energy. Lines are drawn to

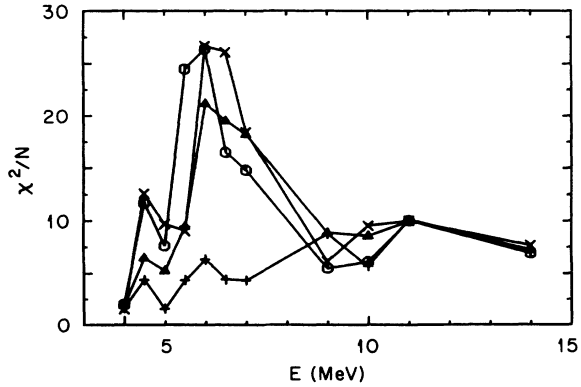

FIG. 8. Best fit values of χ^2/N obtained from least-squares searches on the n + ^{208}Pb scattering distributions for the model *M* and the perturbations *P*1, *P*2, and *P*3 discussed in Sec. V. The symbols are crosses for model *M*, triangles for *P*1, circles for *P*2, and ×'s for *P*3.

connect the points within each set. The crosses are for model M. Our "optimum" designation for this model is supported by the fact that the χ^2/N are as small or much smaller for all energies, except at 9 MeV, than for the searches on any of the three perturbations. The triangles represent the χ^2/N for perturbation $P1$, for which the $h_{9/2}$ partial wave is moved to U. These χ^2/N are larger below 9 MeV than for the optimum model. We note that the increases are very large for 6 to 7 MeV, and we recall from Fig. 6 that the $2h_{9/2}$ state is quasibound near 5 MeV. The circles are for perturbation $P2$, for which the $h_{11/2}$ partial wave is also moved from B to U. The further increase in χ^2/N for energies below 6.5 MeV is consistent with the fact that the $2h_{11/2}$ state is quasibound below the $2h_{9/2}$ state (Figs. 6 and 7). These comparisons of perturbations $P1$ and $P2$ with the optimum model indicate that both the $h_{9/2}$ and $h_{11/2}$ partial waves should be returned to B. Finally, in perturbation $P3$, the $h_{11/2}$ and $h_{9/2}$ orbits are returned to B, and all other partial waves are included in U. From the arguments in Secs. III and IV we expect that those partial waves which have the same lj as do the unoccupied bound states should be kept in B. Indeed, the χ^2/N, which are represented by the symbol "$\times$" in Fig. 8, are much worse than for the optimum model.

We next examine the least-squares adjusted imaginary well depths. These are presented in the upper panels of Figs. 9–12 in terms of volume integrals per nucleon. Figure 9 is for the optimum model M and Figs. 10, 11, and 12 are for the perturbations $P1$, $P2$, and $P3$, respectively.

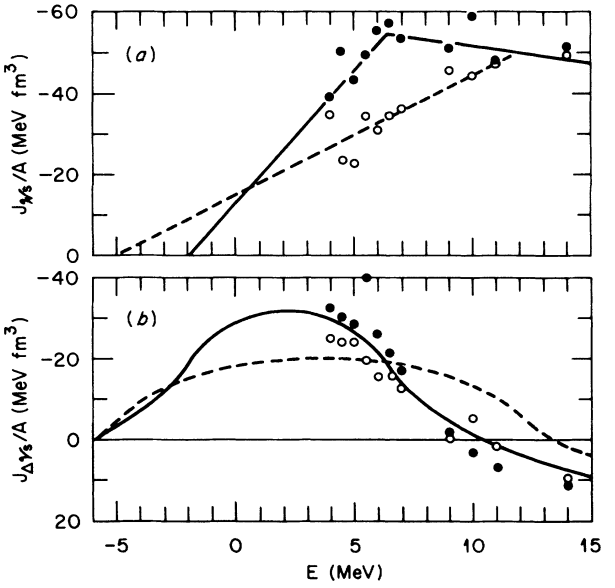

FIG. 9. Volume integrals per particle found for the surface potentials by least-squares searches on the n + ^{208}Pb scattering distributions for model M of Sec. V. The open and solid symbols represent the values for partial wave groups "B" and "U," respectively. In the upper panel the dashed lines for B and the solid line for U are empirical curves from Fig. 22 of Ref. 8. The corresponding curves in the lower panel represent the predicted dispersive volume integrals, also from Fig. 22 of Ref. 8.

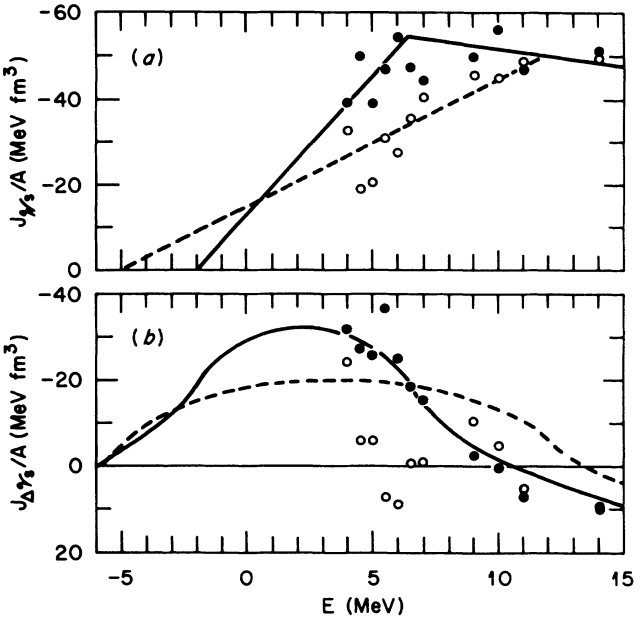

FIG. 10. Volume integrals per particle found for the surface potentials by least-squares searches on the n + ^{208}Pb scattering distributions for perturbation $P1$ of Sec. V. The notations are the same as in Fig. 9.

In each case the open and solid symbols represent, respectively, the values for groups B and U as defined by the M, $P1$, $P2$, or $P3$. In Fig. 9(a) the dashed and solid curves are empirical linear segments which were introduced by JHM (see Fig. 22 of Ref. 8) to describe the average energy dependences for groups B and U, respectively.

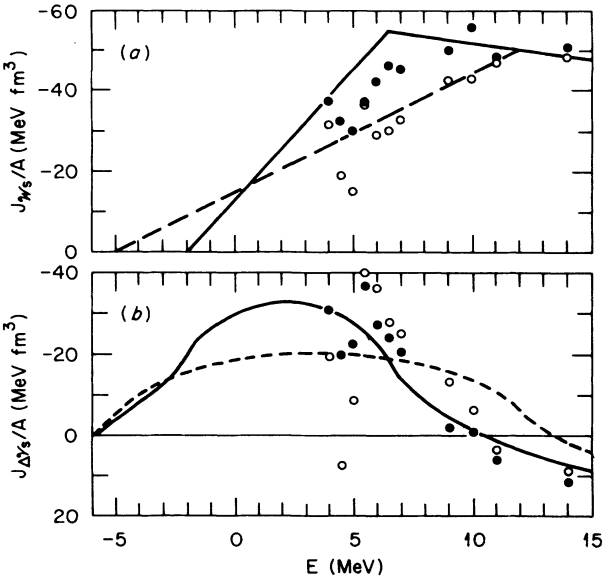

FIG. 11. Volume integrals per particle found for the surface potentials by least-squares searches on the n + ^{208}Pb scattering distributions for perturbation $P2$ of Sec. V. The notations are the same as in Fig. 9.

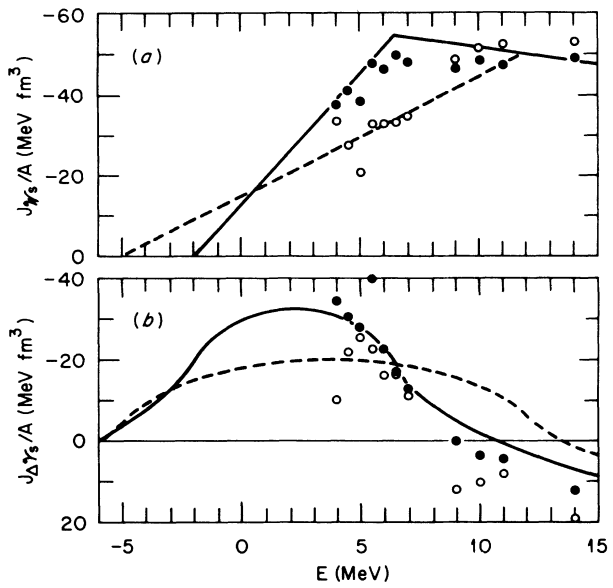

FIG. 12. Volume integrals per particle found for the surface potentials by least-squares searches on the n + ^{208}Pb scattering distributions for perturbation $P3$ of Sec. V. The notations are the same as in Fig. 9.

These curves are reproduced in Figs. 10(a), 11(a), and 12(a).

In Fig. 9(a) for the optimum model, the symbols for groups B and U are well described by the corresponding empirical curves. The significant fact is that, in the energy region from 4 to 10 MeV, the least-squares adjusted depths for the surface imaginary potential are smaller for B than for U. This is a statement regarding averages because each group includes several partial waves; more detailed information is obtained by studying the three perturbations. In Fig. 10(a), for which the $h_{9/2}$ partial wave is moved to U, the depths are seen to be decreased on the average for that group. A reasonable conclusion is that depth is relatively small for $h_{9/2}$. In Fig. 11(a), for which the $h_{11/2}$ partial wave is also moved to U, the depths are further reduced for U. The conclusion is that the depth is also smaller for $h_{11/2}$. In Fig. 12(a) for $P3$ the average depth for U is again smaller than for the optimum model. For this perturbation only the h waves are contained in B. In other words, the partial waves with the same lj as for the unoccupied bound states are now included in U; the fact that the resulting depths are decreased for the perturbed U leads to the conclusion that the depths are smaller, on the average, for partial waves that are associated with the bound states.

This last observation was expected from the discussion of radial nodes in Secs. III and IV. In Fig. 5, for which the imaginary potential was assumed to be independent of l and j, the empirical radius of $\mathcal{W}_s(r;E)$ was found to track the clustered nodes of the partial waves associated with the bound states. In the present case, since the radius is held fixed, the imaginary volume integral must be reduced for those partial waves to maintain small absorption. However, this argument does not apply for the $h_{9/2}$ and $h_{11/2}$ partial waves because these are associated with quasibound states and do not have nodes near the center of $\mathcal{W}_s(r;E)$. Thus it becomes clear why the good fits obtained with the "optimum" model were not achieved[8] by the model with an energy-dependent imaginary radius but without any lj dependences in the depth.

Finally, we examine the least-squares adjusted values of ΔV_s for consistency with the DR constraints. The DR equations for the volume integrals are

$$\Delta J_{\mathcal{V}_{sB}}(E)=\pi^{-1}\int_{-\infty}^{+\infty}dE' J_{\mathcal{W}_{sB}}(E')/(E'-E)\ , \quad (5.8)$$

$$\Delta J_{\mathcal{V}_{sU}}(E)=\pi^{-1}\int_{-\infty}^{+\infty}dE' J_{\mathcal{W}_{sU}}(E')/(E'-E)\ . \quad (5.9)$$

The curves in the lower panels of Figs. 9–12 were calculated by JHM (Ref. 8) under the assumption that the linear segments for the upper panels extrapolate linear to zero and are symmetric about the Fermi energy of -6 MeV. Our discussion is based on the fact that, if the parametric form of $\mathcal{W}_s(r;E)$ is poorly chosen, the parameters for $\Delta\mathcal{V}_s(r;E)$ will be erroneously adjusted to compensate for the poor parametrization and will not be consistent with the DR constraint. This logic requires that the parameters for the other real and imaginary components be well chosen. We believe they are; the volume imaginary component is small[8] at these energies, the volume real component includes the DR constraint and provides a good description[8] of data from -20 to 165 MeV, and the spin-orbit component yields good descriptions[8] of observed spin-orbit effects at both positive and negative energies.

We first examine our optimum model by reference to Fig. 9(b). For $E<9$ MeV the fitted dispersive terms agree well with the DR constraints. The good agreement in that energy region is important for our conclusions regarding the $h_{11/2}$ and $h_{9/2}$ partial waves because that is the energy region of the $2h_{9/2}$ and $2h_{11/2}$ quasibound states. For perturbation $P1$, Fig. 10(b), the $h_{9/2}$ partial wave is omitted from B. We see that the least-squares adjusted $J_{\mathcal{V}_s}/A$ for B are now inconsistent with the DR constraint for 5.5 to 7 MeV. In Fig. 11(b) the symbols represent the fitted values for $P2$, for which both $h_{11/2}$ and $h_{9/2}$ are removed from group B. The disagreement now has a different character; the least-squares adjusted values of $J_{\mathcal{V}_s}/A$ are erratic for energies from 4 to 7 MeV. In Fig. 12(b), for which only $h_{11/2}$ and $h_{9/2}$ remain in group B, the degree of consistency with the DR constraint for group B is better than for $P1$ or $P2$, but still not as good as for the optimum model M. This relative improvement achieved by returning $h_{11/2}$ and $h_{9/2}$ to group B suggests that the real dispersive term is more crucial for locating the nearby quasibound $2h_{11/2}$ and $2h_{9/2}$ states (see Figs. 6 and 7) than it is for the more distant bound states. In summary, the best consistency with the DR constraint for the energy region near the $2h_{9/2}$ and $2h_{11/2}$ quasibound states is achieved for the model which has a separate, relatively weak, imaginary potential for partial waves associated with both quasibound and bound single-particle states.

In the energy region from 9 to 14 MeV the least-

squares adjusted dispersive terms for group B for both the model and the three perturbations are in poor agreement with the DR constraint. A possible explanation is obtained by examining the original searches by JHM.[8] In Fig. 22(b) of JHM, which is similar to our Fig. 9(b), there is good agreement with the DR constraint. However, those were six-parameter searches in which the dispersive diffuseness parameter a_d was varied. For energies near 10 MeV the fitted a_d were very large, about 3 fm, whereas we have set a maximum value of 0.58 fm. A reasonable conclusion is that our approximation of a derivative Woods-Saxon shape with $a_d = 0.58$ fm for $\mathcal{V}_s(r;E)$ is a poor approximation for energies near 10 MeV.

Further empirical evidence[8] supporting the "optimum" model comes from the volume components of the potential. One can expect that a poorly chosen parametrization of $\mathcal{W}_s(r;E)$ would also be reflected in the least-squares adjusted depth of the real volume component if that depth, V_v were also varied in the search. The DR constraint for the volume component predicts a plateau in V_v near 10 MeV as a consequence of an inflection in the energy dependence in the imaginary volume depth. In JHM (Ref. 8) the depth V_v was varied in searches with three models, namely, a "fixed-geometry" model, an "energy-dependent–surface-geometry" model, and the "angular-momentum-dependent" model. The least-squares adjusted V_v for the first two models showed relatively poor agreement with the plateau, but the V_v for the last model, which is the forerunner of the present model, showed good agreement. [See Figs. 2(b), 16, and 20 of Ref. 8.]

VI. CONCLUSIONS

For neutron energies of a few MeV, energy dependences have been reported[1–3,8] for the radius and diffuseness of the surface imaginary component of the optical model potential for n + ^{89}Y and n + ^{208}Pb. We point out that the empirical dependences for the radius are essentially the same as the dependences on energy of the positions of the surface radial nodes of partial waves that have the same l and j as do the bound unoccupied single-particle states. In other words, the imaginary potential "tracks" those nodes. This implies that essentially equivalent models can be developed by use of a constant imaginary radius, providing that those partial waves which have the same lj as the bound states have a different imaginary depth than do other partial waves. This equivalence is demonstrated in Sec. III using the specific example of 5-MeV neutrons on ^{89}Y.

For the case of n + ^{208}Pb, Johnson, Horen, and Mahaux[8] improved the fits to the data for $E < 10$ MeV by a model which has a constant imaginary radius and a particular angular momentum dependence in the depth of the potential. Their discussion was empirical with no reference to the bound unoccupied single-particle states. We have studied their model further by making a sequence of comparisons with perturbations of the model for which we examine the quality of fits to the data, the variations in the imaginary potentials, and the consistency of the least-squares adjusted surface real depths with the dispersion relation constraint. We find that an essential character of their model[8] is that the partial waves having the same lj as do the $2h_{11/2}$ and $2h_{9/2}$ states, which are quasibound by the centrifugal barrier, are grouped together with partial waves having the same lj as do the bound unoccupied single-particle states. For $E < 10$ MeV, the depth of the imaginary potential for the partial waves in this "bound and quasibound" group are smaller than for other partial waves.

The partial waves having the same lj as the bound and quasibound orbitals consist of the s, d, g, h, $i_{11/2}$, and $j_{15/2}$ partial waves. Actually, the data do not contain enough information to establish with certainty that every one of the partial waves associated with the unoccupied bound states must be included in this group. In particular, the s-wave component contributes relatively little to the scattering cross section and there is some evidence[8,14] from low-energy s-wave scattering that it should not be included in the group. A conservative conclusion is that for neutron energies from 4 to 10 MeV the partial waves for $l = 2$, 4, and 5 have smaller imaginary potentials than do the partial waves with $l = 1$ and 3.

This model cannot be replaced by one which has an energy-dependent radius but does not have an lj dependence, because the radial nodes of the scattering waves having the same lj as do the bound states are not clustered about the same radius as are the nodes associated with the quasibound states. Also, since the bound and quasibound states are of opposite parity (except for the bound $j_{15/2}$ state), a model which groups the partial waves according to parity will not give as good a description of the scattering data.

The grouping together of partial waves corresponding to the bound and quasibound states is a simple concept. However, it is an unexpected result. Our study gives compelling evidence that the quasibound $2h_{11/2}$ and $2h_{9/2}$ states are important for neutron scattering from ^{208}Pb for $E < 10$ MeV. It is reasonable to expect quasibound states to have a significant influence on low energy nucleon scattering from other nuclei.

ACKNOWLEDGMENTS

We are grateful for stimulating discussions with Dr. C. Mahaux and Dr. G. R. Satchler. Research was partially supported by the U.S. Department of Energy under Contract No. DE-FG02-87ER40326. Oak Ridge National Laboratory is operated by Martin Marietta Energy Systems, Inc. for the U.S. Department of Energy under Contract No. DE-AC05-840R21400.

*Permanent address: Denison University, Granville, OH 43023.
[1]R. W. Finlay, J. R. M. Annand, J. S. Petler, and F. S. Dietrich, Phys. Lett. **155B**, 313 (1985); **157B**, 475 (1985).
[2]J. R. M. Annand, R. W. Finlay, and F. S. Dietrich, Nucl. Phys. **A443**, 249 (1985).
[3]R. D. Lawson, P. T. Guenther, and A. B. Smith, Phys. Rev. **34**, 1599 (1986).
[4]N. C. Francis and K. W. Watson, Am. J. Phys. **21**, 659 (1953); N. F. Mott and H. S. W. Massey, *Theory of Atomic Collisions,* 3rd ed. (Oxford University Press, Oxford, 1965).
[5]A. M. Lane, J. E. Lynn, E. Melkonian, and E. R. Rae, Phys. Rev. **2**, 424 (1959).
[6]P. A. Moldauer, Nucl. Phys. **47**, 65 (1963).
[7]P. G. Young, in *Use of the Optical Model for the Calculation of Neutron Cross Sections Below 20 MeV,* NEA Nuclear Data Committee-222 'U' (Paris, 1986) (OECD Nuclear Energy Agency, Paris, France), p. 127.
[8]C. H. Johnson, D. J. Horen, and C. Mahaux, Phys. Rev. C **36**, 2252 (1987).
[9]C. Mahaux and H. Ngo, Nucl. Phys. **A378**, 205 (1982).
[10]J. Rapaport, T. S. Cheema, D. E. Bainum, R. W. Finlay, and J. D. Carlson, Nucl. Phys. **A296**, 95 (1987).
[11]C. E. Floyd, Ph.D. dissertation, Duke University, 1981 (unpublished).
[12]J. P. Delaroche, C. E. Floyd, P. P. Guss, R. E. Byrd, K. Murphy, G. Tungate, and R. L. Walter, Phys. Rev. C **28**, 1410 (1983).
[13]J. P. Jeukenne (private communication).
[14]D. J. Horen, C. H. Johnson, J. L. Fowler, A. D. MacKellar, and B. Castel, Phys. Rev. C **34**, 429 (1986).